Two-step Mott transition in Ni(S,Se)$_2$: μSR studies and charge-spin percolation model

Qi Sheng,[1] Tatsuya Kaneko,[1,2] Kohtaro Yamakawa,[1] Zurab Guguchia,[1] Zizhou Gong,[1] Guoqiang Zhao,[1,3]
Guangyang Dai,[3] Changqing Jin,[3] Shengli Guo,[4] Licheng Fu,[4] Yilun Gu,[4] Fanlong Ning,[4] Yipeng Cai,[5] Kenji M. Kojima,[5]
James Beare,[6] Graeme M. Luke,[5,6] Shigeki Miyasaka,[7] Masato Matsuura,[8] Shin-ichi Shamoto,[8,9] Takashi Ito,[9]
Wataru Higemoto,[9] Andrea Gauzzi,[10] Yannik Klein,[10] and Yasutomo J. Uemura[1,*]

[1]*Department of Physics, Columbia University, New York, New York 10027, USA*
[2]*RIKEN Center for Emergent Matter Science (CEMS), Wako, Saitama 351-0198, Japan*
[3]*Institute of Physics, Chinese Academy of Sciences, Beijing 100190, China*
[4]*Department of Physics, Zhejiang University, Hangzhou 310027, China*
[5]*TRIUMF, Vancouver, British Columbia, V6T 2A3 Canada*
[6]*Department of Physics and Astronomy, McMaster University, Hamilton, Ontario, L8S 4M1 Canada*
[7]*Department of Physics, Osaka University, Toyonaka, Osaka 560-0043, Japan*
[8]*Neutron Science and Technology Center, Comprehensive Research Organization for Science and Society (CROSS),
Tokai, Ibaraki 319-1106, Japan*
[9]*Advanced Science Research Center, Japan Atomic Energy Agency (JAEA), Tokai, Naka, Ibaraki 319-1195, Japan*
[10]*Institut de Minéralogie, de Physique des Matériaux et de Cosmochimie (IMPMC), Sorbonne Université,
CNRS, IRD, MNHN, 4 place Jussieu 75005 Paris, France*

A pyrite system NiS$_{2-x}$Se$_x$ exhibits a bandwidth controlled Mott transition via (S,Se) substitutions in a two-step process: the antiferromagnetic insulator (AFI) to antiferromagnetic metal (AFM) transition at $x \sim 0.45$ followed by the AFM to paramagnetic metal (PMM) transition at $x \sim 1.0$. Among a few other Mott systems which exhibit similar two-step transitions, Ni(S, Se)$_2$ is of particular interest because a large intermediate AFM region in the phase diagram would provide unique opportunities to study the interplay between the spin and charge order. Muon spin relaxation (μSR) measurements on NiS$_{2-x}$Se$_x$ have been carried out on seven different Se concentrations from $x = 0$ to 1.0. The results on quantum evolution demonstrate significantly random spin correlations in the AFM region associated with a rapid reduction of the average local static Ni moment size with increasing x, yet without signatures of macroscopic phase separation as confirmed by nearly full volume fraction participating in the static muon relaxation process up to $x \sim 0.9$ at low temperatures. The observed time spectra in the AFM region indicate Lorentzian distribution of static internal field expected for a spatially dilute spin structure. No signature of dynamic critical behavior was observed in thermal phase transitions. The previous neutron scattering studies found sharp magnetic Bragg peaks with a slower reduction of the average ordered moment size in the AFM region. By comparing and combining the muon and neutron results, here we propose a picture where the spin order is maintained by the percolation of "nonmetallic" localized and dangling Ni moments surrounded by S, while the charge transition from AFI to AFM is caused by the percolation of the conducting paths generated by the Ni-Se-Ni bonds. This model of interpenetrating charge and spin percolation captures the behavior of experimental results on (a) Se concentration for the insulator to metal transition, (b) Se concentration for the AFM to PMM transition, (c) variation of Hall effect in the AFM region due to conducting Ni charges on the backbone of the percolating charge network, (d) evolution of the neutron Bragg intensity, (e) evolution of the muon static local fields, and (f) spatial variation of the local conductance observed by STM.

I. INTRODUCTION

Mott transition [1] is one of the most important manifestations of strong electron correlations in solids, playing important roles in magnetic order and metallic and superconducting charge conduction in many emergent quantum materials [2], including high-T_c cuprates and twisted graphene [3]. Mott metal-insulator transitions in prototypical systems RENiO$_3$ (RE = rare earth) and V$_2$O$_3$ occur in a single-step process from antiferromagnetic insulator (AFI) to paramagnetic metal (PMM) state in quantum evolution. The transition
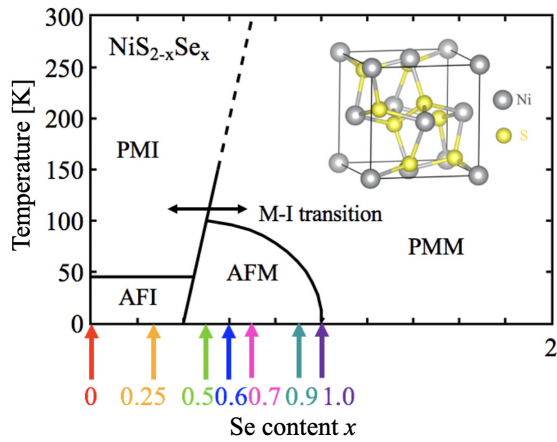
FIG. 1. Phase diagram of $NiS_{2-x}Se_x$. Color-coded arrows show specimens examined. Inset shows the crystal structure of NiS_2.

in these systems is also associated with a simultaneous structural phase transition [4] and the thermal hysteresis in the magnetic order parameter was observed [5]. Recent studies of spatially resolving optical responses [6,7] found the thermal evolution of Mott transition in V_2O_3 and VO_2 associated with mesoscopic phase separation between AFI and PMM states with the typical length scale of ∼100–500 nm. Muon spin relaxation [8,9] is another powerful probe to study phase separation between magnetically ordered and paramagnetic volumes. μSR results in RENiO$_3$ [10,11] with RE substitutions and V_2O_3 in ambient and hydrostatic pressure [11,12] demonstrated that thermal and quantum transitions occur with phase separation and thermal hysteresis, thus confirming the first-order nature of Mott transitions in these systems.

Following RENiO$_3$ and V_2O_3 [11], a part of the present authors extended the μSR studies to Mott transitions in BaCoS$_2$ with a bandwidth tuning via hydrostatic pressure, and in Ba(Co, Ni)S$_2$ with a filling control via (Co,Ni) substitutions [13]. Both ways of tuning lead to a two-step quantum evolution of AFI to antiferromagnetic metal (AFM) to PMM states without structural phase transition. Although a clear indication of phase separation and absence of dynamic critical behavior were observed in these cases, it was not possible to elucidate details of the interplay between charge and spin orders, limited by a very narrow intermediate AFM region in the phase diagrams.

A pyrite Mott insulator NiS_2 also shows the two-step AFI-AFM-PMM evolution both in the (S,Se) substitution without structural transition and application of hydrostatic pressure with a structural transition [14–17]. In $NiS_{2-x}Se_x$ with Se having a larger atomic size as compared to S, the lattice constant increases with increasing Se concentrations. Ni-Se and Se-Se bonds are, however, stronger than Ni-S and S-S bonds due to Se orbitals being more extended than S orbitals. As shown in DMFT calculations [18,19], this lowers the energy level of the antibonding Se-Se orbital and results in high overlap with the lower Hubbard band of Ni e_g orbitals. In this way, the (S,Se) substitutions promote metallic conduction and result in Mott insulator-metal transition in a charge-transfer salt. As shown in Fig. 1, the AFI to AFM transition in $NiS_{2-x}Se_x$ occurs around Se concentration $x \sim 0.45$, while the AFM to

PMM transition and the loss of static magnetic order takes place around $x \sim 1.0$, and the PMM phase extends up to the end compound $NiSe_2$ which still has the pyrite structure. A relatively large AFM region and availability of high-quality poly and single-crystal specimens have enabled extensive studies of this system with transport [20], x-ray [21], neutron [22–24], Mössbauer effect [25,26], optical [27], and STM [28] methods. In the present work, we will add μSR measurements on seven different Se concentrations (see Fig. 1), and elucidate the evolution of spin orders.

Comparison and combination of the results from muon and neutron studies will lead us to propose a picture based on the charge and spin percolation on NiS_2 network with a random (S,Se) substitution. Applicability of the concept of percolation on NiS_2 was hinted by a spatial inhomogeneity found by STM in a Ni(S, Se)$_2$ crystal near the AFI-AFM border, and was recently discussed [29] for explaining the metal to insulator transition as the result of percolation of charge conduction path, with respect to the nearest neighbor Se-Se bonds which connect adjacent (S, Se)$_6$ octahedral cages surrounding Ni. In the present work, we consider individual Ni-Se-Ni conduction paths, and also apply the percolation concept to a spin network of nonconducting localized or dangling Ni atoms surrounded by S$_6$ or S$_5$Se cages. A satisfactory agreement between the results of the Monte Carlo simulation of this model and experimental findings will lead us to propose the interpenetrating charge-spin percolation as a picture to explain how metallicity and static magnetic order coexist in the AFM state in this material.

II. METHODS

$NiS_{2-x}Se_x$ possesses a cubic pyrite system in which the Ni and (S, Se)$_2$ atoms bond to form a 3d rock-salt type lattice. Since the crystal structure is composed of [Ni(S, Se)$_2$]$_3$ octahedra that create face-centered cubic Ni sites, the strong p-orbital hybridization between S and Se atoms forces the (S, Se)$_2$ cluster to have a charge configuration of -2 and therefore making Ni also divalent [21,24,28]. NiS_2 is an insulator with $S = 1$ Ni moments ordering antiferromagnetically below $T \sim 40$ K [23,30]. Note that the ordered Ni moment size $1.0 \sim 1.2\mu_B$ determined by neutron scattering [23,24,30] is reduced to about a half of the nominal $S = 1$ moment, which may be related to the geometrical frustration of an FCC antiferromagnet [31]. As NiS_2 is doped with Se atoms, the system is driven to a bandwidth-controlled MIT and exhibits magnetic ordering even in the metallic state. Broadening of the bandwidth due to isovalent (S, Se) substitutions causes the metal-insulator transition into the AFM state and subsequently to the PMM state [20] as shown in the phase diagram of Fig. 1.

Polycrystalline pellets of $NiS_{2-x}Se_x$ with $x = 0$, 0.25, 0.5, 0.7, 0.9, and 1.0 were prepared by chemical vapor transport methods. A single-crystal specimen of $NiS_{2-x}Se_x$ with $x = 0.6$ was prepared according to methods described elsewhere [23] and was used in neutron studies. μSR measurements were conducted at the Centre for Molecular and Materials Science at TRIUMF in Vancouver, Canada, using the LAMPF and Nutime spectrometer with a helium gas-flow cryostat with accessible temperatures down to ∼2 K. The μSR analysis was
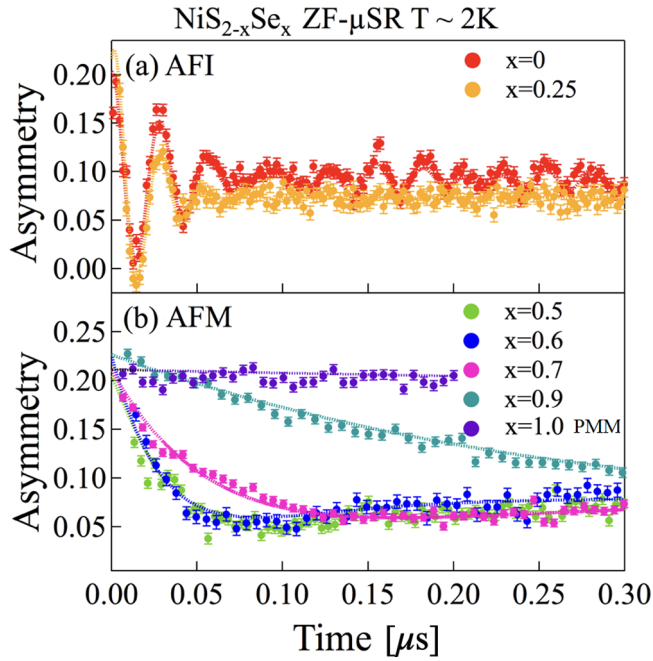
FIG. 2. Zero-field (ZF) μSR spectra showing asymmetry versus time in NiS$_{2-x}$Se$_x$ at the base temperature $T \sim 2$ K, with (a) showing results of $x = 0, 0.25$ in the AFI region and (b) showing $x = 0.5$, 0.6, 0.7, and 0.9 in the AFM region. Color code of Fig. 1 is followed.

performed in the time domain using the program MUSRFIT [32].

III. μSR EXPERIMENTAL RESULTS AND DISCUSSIONS

In Fig. 2, we show the μSR time spectra observed in zero field (ZF) at the base temperature ($T \sim 2$ K) in different specimens of NiS$_{2-x}$Se$_x$. Along the vertical axis, we plot asymmetry, which is proportional to the projection of the polarization of the muon. For $0 \leqslant x \leqslant 0.5$ samples, function

$$A_{\text{sample}} = \frac{2}{3} \cos\left(2\pi \nu t + \frac{\pi \phi}{180}\right) e^{-\lambda t} + \frac{1}{3} e^{-\frac{1}{T_1}t} \quad (1)$$

is used to fit the sample signal. For $x = 0.0$, three different oscillation frequencies were observed. A long-lived oscillation was observed in $x = 0.0$ and 0.25, while a rapid exponential-like relaxation of the oscillation was observed in $x = 0.5$. This may originate from the bandwidth-controlled MIT that occurs around $x = 0.45$ [20].

For the $x \geqslant 0.6$ compounds, the μSR spectra fit well to the known shape for the case of dilute alloy spin glasses [9,33]. The fitting function used for the sample signal is

$$A(t) = \frac{2}{3}(1 - at)e^{-at} + \frac{1}{3}. \quad (2)$$

Appendix A shows a subttle difference between the time spectra for the $x = 0.5$ and 0.6 compounds, which led to different choices of the fitting functions for these systems. The decay rate a of the "spin-glass" function becomes smaller with increasing Se doping x.
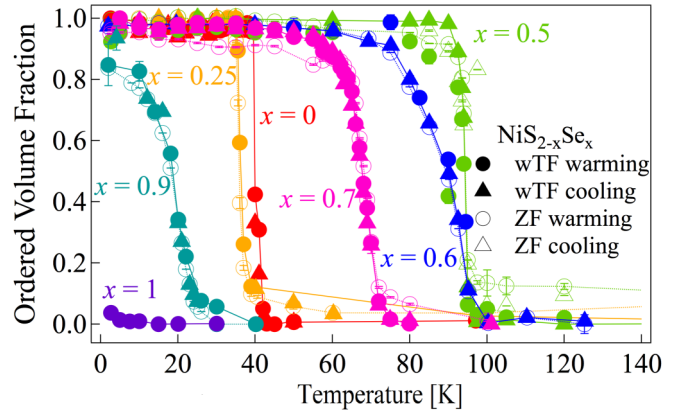

FIG. 3. The volume fraction of the magnetically ordered regions determined by μSR. Closed symbols and open symbols are showing data in wTF and ZF, respectively. Color code of Fig. 1 is followed.

Before going into detail about the shape of the relaxation function, which may involve the internal field homogeneity and the size of moments, we present the ordered volume fraction in Fig. 3. The volume fraction of the magnetically ordered region is derived from the "paramagnetic" response in a weak transverse field (wTF) of $\sim$3 mT and from the ZF time spectra. The thermal phase transition occurs sharply without any clear signs of thermal hysteresis in the $0 \leqslant x \leqslant 0.5$ region, while a more gradual evolution of the ordered volume was observed for higher Se concentrations in the AFM region. At low temperatures, all the specimens up to $x = 0.9$ develop magnetic order in nearly full volume fraction.

Open symbols in Fig. 4 show the strength of the static internal field observed in ZF μSR. This static field is obtained by

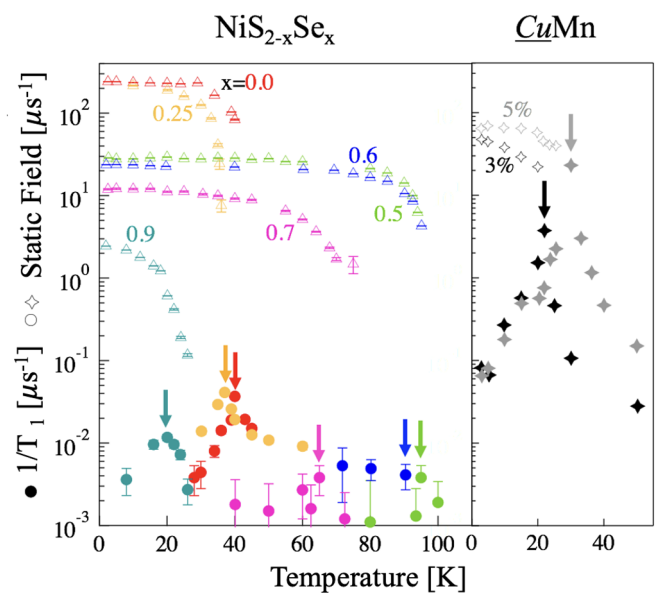$$B_{\text{avg}} = \sqrt{(\Delta B)^2 + B^2}, \quad (3)$$

FIG. 4. The static internal field in ZF and the dynamic relaxation rate $1/T_1$ in LF in NiS$_{2-x}$Se$_x$ and $\underline{Cu}$Mn spin glasses [33]. Colored arrows are showing the Néel temperature.
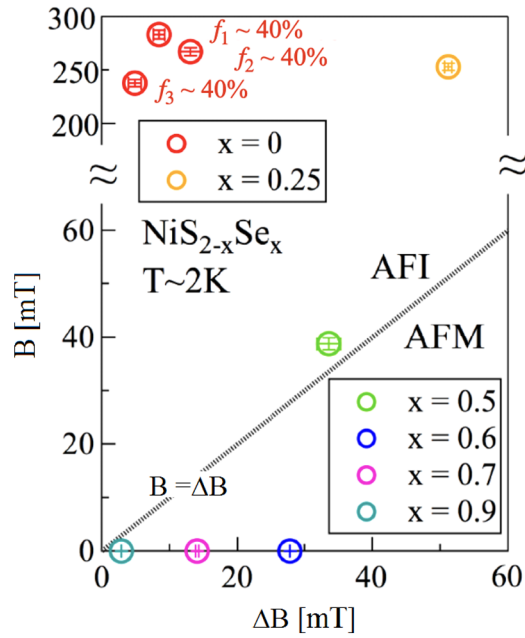
FIG. 5. Precession field B and the width ΔB at a temperature $T \sim 2$ K in ZF μSR.

where B is the precession field and ΔB is the field width, representing the static local ordered moment. The width of the distribution of the internal field is calculated by $\Delta B = \lambda/\gamma_\mu$ for $0 \leqslant x \leqslant 0.5$ samples and $\Delta B = a/\gamma_\mu$ for $x \geqslant 0.6$ samples, where $\gamma_\mu/2\pi = 0.1355$ MHz/mT, λ is the decay rate in Eq. (1) and a is the decay rate in Eq. (2). A clear reduction of the moment size with increasing Se doping is observed.

We also compare B and ΔB observed at the base temperature ~ 2 K in ZF for different Se dopings, which is shown in Fig. 5. In Fig. 5, the vertical axis represents the precession field B while the horizontal axis represents the field width ΔB. This figure indicates that the ZF time spectra exhibit underdamped oscillation in the AFI phase, which develops into the overdamped "spin-glass" like responses in the AFM state. This can also be seen in Fig. 2.

Closed symbols in Fig. 4 show the temperature dependence of dynamic relaxation rate $1/T_1$ in μSR under longitudinal field (LF) through the thermal phase transition. The dynamic relaxation rate $1/T_1$ is observed under LF = 300, 250, 70, 100, 30, and 10 mT for $x = 0$, 0.25, 0.5, 0.6, 0.7, and 0.9, respectively, which are comparable to the static field strength of each specimen at ~ 2 K. Almost no signature of dynamic critical behavior is observed at the Néel temperature shown by the colored arrows. This can be seen by comparing our results with some typical systems that exhibit critical divergence of $1/T_1$ in μSR via second-order phase transition. The right part of Fig. 4 shows the results of dilute-alloy spin glasses $\underline{Cu}$Mn and $\underline{Au}$Fe [33] systems which exhibit variation of $1/T_1$ in a few orders of magnitude toward the transition temperature T_g. It is safe to say that the absolute values and the variable range of $1/T_1$ in NiS$_{2-x}$Se$_x$ are much smaller, which suggests first-order thermal phase transition without critical spin dynamics in NiS$_{2-x}$Se$_x$.

Motivated by the ZF μSR time spectra in the AFM region of NiS$_{2-x}$Se$_x$ being similar to those observed in dilute alloy

spin glasses, we performed measurements of dc and ac susceptibility of the NiS$_{2-x}$Se$_x$ specimens, finding no signatures of typical spin glasses such as a sharp peaking of the ac susceptibility at T_g. Together with the absence of dynamic critical behavior shown in Fig. 4, the observed magnetism of the AFM state seems to be significantly different from the known cases of random spin systems.

In summary, the present μSR results revealed previously unknown features of static magnetism in the AFM state in NiS$_{2-x}$Se$_x$. The spin correlation is highly disordered, and the static local moment size is reduced rapidly with increasing doping x, leading to complete elimination of static magnetism in the PMM state. The volume fraction of the ordered region is nearly full until very close to the boundary of AFM and PMM states. No dynamic critical behavior was observed in thermal phase transitions in the AFM region, common to the cases found in Ba(Co, Ni)S$_2$ [13] and in the AFI phases of V$_2$O$_3$ and RENiO$_3$ [11]. In contrast to V$_2$O$_3$ and RENiO$_3$, in which the magnetic order is destroyed via the reduction of ordered volume fraction in quantum tuning, the static magnetic order in NiS$_{2-x}$Se$_x$ is destroyed via the decrease of the ordered moment size in the AFM region.

IV. DIPOLAR FIELD SIMULATIONS

A. Comparisons of μSR and neutron results

The μSR time spectra observed for the $x = 0.6$ sample exhibit overdamped "spin-glass" like responses as shown by the dark blue line in Fig. 2. However, an earlier neutron scattering study on NiS$_{2-x}$Se$_x$ [23] reported the observation of the antiferromagnetic Bragg peak even in the AFM region, including the same $x = 0.6$ single crystal examined by μSR. The difference between neutron scattering and μSR experimental results in the AFM region of NiS$_{2-x}$Se$_x$ can be seen clearly in the left two columns of Fig. 6. They compare the neutron ordered moment size calculated from neutron Bragg intensity [panel (a)] and the average static local field strength B_{avg} determined from μSR data and calculated by Eq. (3) [panel (c)], of which the B_{avg} shows a more rapid decrease in the AFM region. Panel (b) shows the half-width at half maximum (HWHM) of the M1 antiferromagnetic (AF) Bragg peak which gives the upper limit of the inverse correlation length κ, and panel (d) shows the ratio of the distribution of the field ΔB over the magnitude of the field B_{avg}, $\Delta B/B_{avg}$. With increasing x, the AF correlation length remains virtually unchanged (or resolution-limited) as detected by the HWHM of the Bragg peaks, however, the increasing ratio $\Delta B/B_{avg}$ derived from the μSR data indicates a wider distribution of Ni moment sizes in NiS$_{2-x}$Se$_x$ system.

B. Determination of the muon sites

To reconcile the apparently contradicting results of the AFM state of the NiS$_{2-x}$Se$_x$ system from the μSR and neutron scattering experiments, internal field simulations were performed on $20 \times 20 \times 20$ supercell to check the μSR responses with given spin structures. Lattice parameters and spin structures from Ref. [24] were used. Because previous neutron results [23,24] consistently indicate that only the type I (M1) magnetic structure neutron response was observed in the AFM
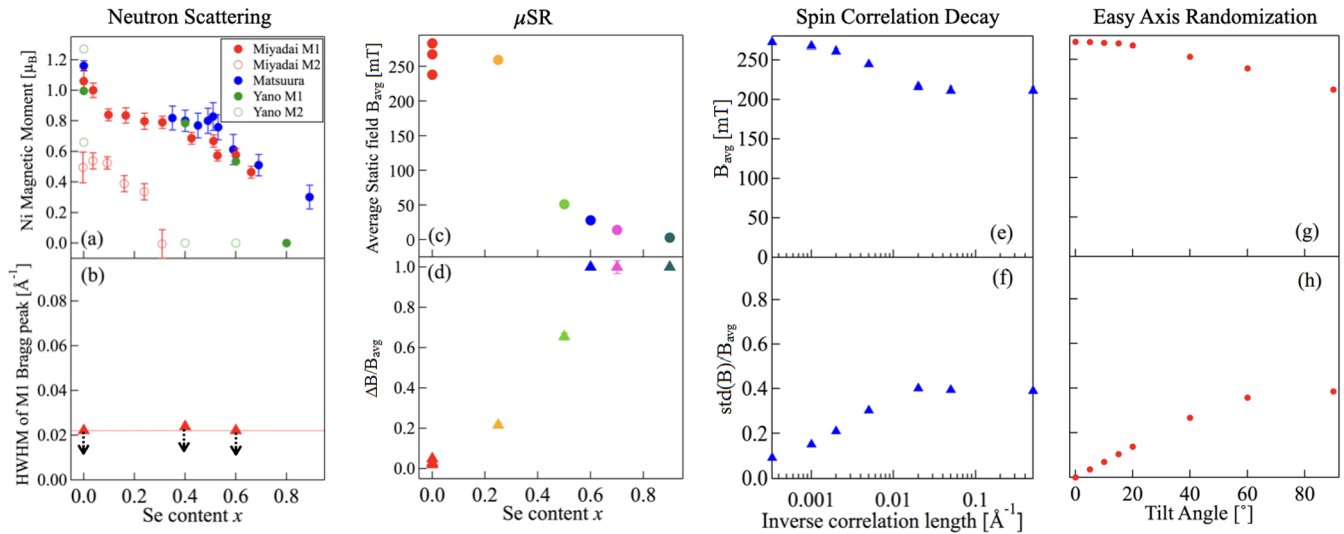
FIG. 6. [(a)–(d)] Comparison of neutron scattering and μSR experimental results on NiS$_{2-x}$Se$_x$ system: (a) Ni magnetic moment calculated from Bragg intensity from previous neutron studies about NiS$_{2-x}$Se$_x$ system, data adapted from Miyadai *et al.* 1983, Matsuura *et al.* 2000 and Yano *et al.* 2016 (Refs. [22–24]). (b) HWHM from M1 Bragg intensity vs Se content. Data estimated from Yano *et al.* 2016 (Ref. [24]). The red triangles and dashed line show the upper limit of the inverse correlation length κ, and the black downward error bars show the possible range of the actual inverse correlation length after taking the instrumental resolution into account. (c) The change of average static local field strength B_{avg} with Se doping. (d) The change of $\Delta B/B_{\mathrm{avg}}$ with Se doping. [(e)–(h)] Comparison of the simulation results for AF spin correlation decay and easy axis tilt: (e) and (f) show the change of the simulated muon average field B_{avg} the ratio of the simulated field distribution width ΔB over the simulated muon average field B_{avg}, $\Delta B/B_{\mathrm{avg}}$, with respect to the change of the inverse correlation length κ, respectively. (g) and (h) show the change of values corresponding to (e) and (f) with respect to the change of the easy axis rotating angle θ.

state with $x = 0.5$–0.7, we only calculate results of the M1 spin structure in our following discussion.

The estimate of the internal field observed by muon spin relaxation involves two features. One is the determination of the muon location in the crystal structure, which was calculated to be the EPsite $= (0.07, 0.21, 0.32)$ as shown in Fig. 7(a). We employed electrostatic (Hartree + Core) potential available from the standard density functional theory (DFT) calculation code VASP, for a hydrogen plus NiS$_2$ system without relaxing the lattice structure. The other feature is the character of the coupling between the dipolar moment of Ni and the muon. Generally, the isotropic hyperfine coupling parameter (A_{iso}) and the dipolar-field coupling (B_{dip}) are the main characters. Here, we are interested in the broadening of the internal fields, where the dipolar field will be the main cause. Assuming the type I (M1) structure of Ni moments, the dipolar field of NiS$_2$ calculated at muon site EP is 274 mT, agreeing well with the μSR experimental result of the pure compound $\sim$270 mT.

C. Simulation of the local fields at the muon site: effects of the spin correlation length and easy-axis randomization

Firstly, we capture the influence of long-range spin correlation length ξ on the muon detected field by estimating the local field distribution with different inverse correlation length $\kappa = 1/\xi$ values. Using the Monte Carlo method by performing 50 000 independent trials of dipolar sums at the muon EPsite, it is found that the resulting dipolar field approximately follows the Gaussian distribution. As κ increases (thus the correlation length ξ decreases), the mean-field decreases whereas the field distribution width increases, as shown in Figs. 6(e) and 6(f). According to the neutron Bragg peak width

shown in panel (b), the upper limit of κ for the $x = 0.6$ sample is $\sim$0.02 Å^{-1} and remains approximately unchanged with Se doping, which will lead to a $std(B)/B_{\mathrm{avg}}$ ratio of less than
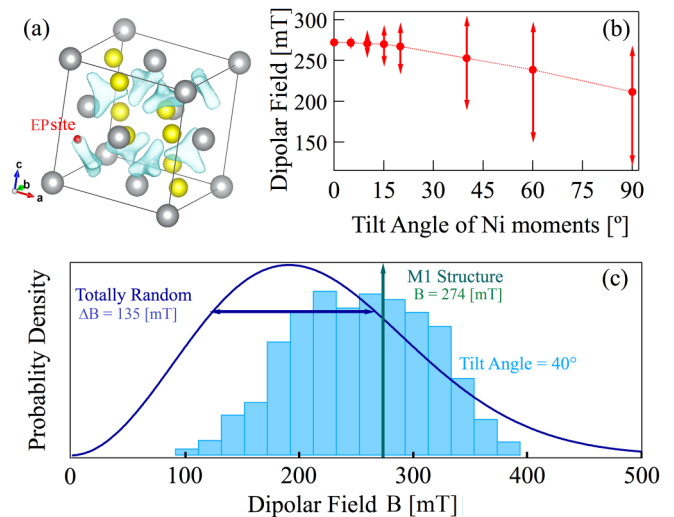

FIG. 7. (a) Electrostatic potential map calculated for the AFM state of NiS$_2$. Blue isosurfaces possess electrostatic potential $\sim$0.3 eV above the potential minimum. The red point shows the position of the electrostatic potential (EP) site $= (0.07, 0.21, 0.32)$. (b) Mean value of the dipolar field versus the Ni moments tilt angle θ. Standard deviations of field distribution are shown by the vertical arrows. (c) The dark blue curve shows the field distribution under the maximum randomness. A light blue histogram shows the simulated field distribution with tilt angle $\theta = 40°$. Green Arrow shows the calculated dipolar field with M1 structure for NiS$_2$.

0.4 according to the simulation results shown in panel (f). This estimated $\Delta B/B_{avg}$ ratio is significantly smaller than the actual value of $\sim$0.7 for the $x = 0.6$ sample as shown in panel (d). Thus the AF correlation length variation cannot account for the largely reduced and broadened muon local field in the AFM region.

Then, we check the local field change with the possible doping evolution of easy axis orientation. Similar to the AF correlation length variation, the effect of easy axis tilt on the muon local field was estimated by the Monte Carlo method. Distribution of the local field for different values of θ are summarized in Figs. 7(b) and 7(c). The light blue histogram in Fig. 7(c) shows the approximately Gaussian distribution of the dipolar field with $\theta = 40°$. As the tilt angle θ increases, corresponding to the more random easy axis, the field distribution shifts towards decreasing mean value of the field and wider distribution width, as shown in panel (b) of Fig. 7. For the case that the Ni moments are random as in a spin glass case, the field distribution possesses a field width of $\Delta B = 135$ mT, as shown by the dark blue curve in Fig. 7(c). The field distribution in any configuration should always fall between the M1 field (green arrow) and the random limit (dark blue curve) shown in Fig. 7(c).

In the above easy-axis-tilting model, only the dipolar field at the EPsite = (0.07, 0.21, 0.32) is monitored. However, because the mutual spin angles are kept unchanged while the principal axis [1 1 1] is changing, the M1 structure crystal symmetry is broken which could bring about further variations of fields at the other equivalent muon sites. Thus the field distribution on the other equivalent sites was also checked, and it is found that the θ dependence of the dipolar fields are identical whereas the role of the sites are cyclic rotated. This implies that it is sufficient to investigate the θ dependence and the anisotropy of the dipolar tensor on one muon site for evaluating all the Ni spin reorientation effect.

Thus the easy axis randomization simulation result indicates that if the easy axis changes direction, or exhibits the tendency towards "melting," a diminishing average field with the development of the distribution width can be expected, resulting in the damping of the muon spin relaxation spectra, which is similar to the effect of the reduction of the AF correlation length on the muon local field, as compared in Figs. 6(e)–6(h).

For the comparison of neutron Bragg peak intensities for different spin orientations (magnetic easy axis), the terms that are independent of the spin orientations in the partial differential cross-section for magnetic Bragg scattering are ignored and only the magnetic moment component $\vec{S}_j^\perp$ perpendicular to the scattering vector Q is considered. For NiS_2, the M1 structure has the same periodicity with the lattice ($Q = (000)$), but the AF and Nuclear diffraction appears in different Q's, with AF peaks appearing at (001) and (110) [24]. Assuming that Q is parallel to the c axis with scattering vector Q (001), then a rotation of the easy axis by the angle θ within the a-c plane of the crystal won't affect $\vec{S}_j^\perp$. Thus the randomization of the easy axis would not significantly affect the AF neutron Bragg intensities observed due to the cubic structure of NiS_2.

It can be seen that allowing a change of the easy axis from the crystal axis will contribute to the lowered and broadened internal field with Se doping in the AFM region observed
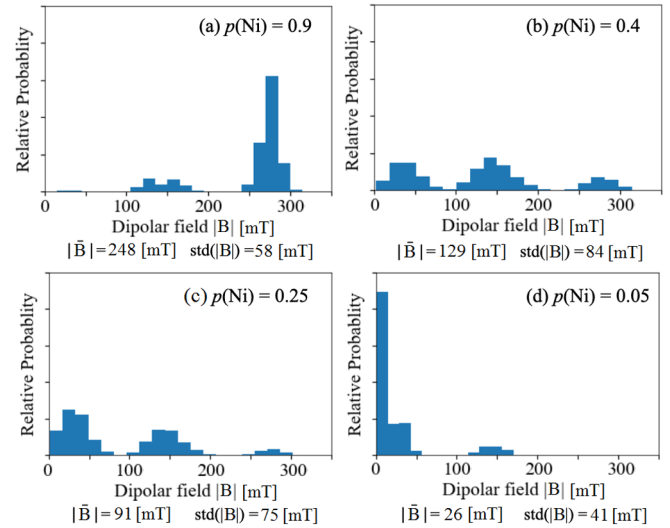

FIG. 8. The simulated field distribution in the case of Ni site "simple dilution" as in the percolation network with the site population (a) $p(\mathrm{Ni}) = 0.9$, (b) 0.4, (c) 0.25, and (d) 0.05.

in the μSR spectrum, while not affecting the neutron intensities. So easy axis randomization can help reconcile the seemingly contradicting μSR and neutron scattering results to some extent. However, there are still significant differences between the simulated local field at the muon site and the observed μSR spectrum. The simulated local field is significantly higher than that observed by μSR in the AFM region of $NiS_{2-x}Se_x$. Also, both the easy axis rotation and the AF correlation length variation from the above simulations will lead to Gaussian distributions of muon local fields, expected in general for dense magnetic systems. The actual ZF-μSR spectrum for $NiS_{2-x}Se_x$ in the AFM region (Se content $x = 0.6$–0.9) exhibit the line shape corresponding to Lorentzian-like field distributions with a broader local field distribution expected in more spatially dilute spin systems.

D. Percolation model for local field

To account for this feature, we involve random Ni site dilution of magnetic moments in our model by assuming a "simple dilution" case with a constant (direction and location-independent) dilution factor $p(\mathrm{Ni})$, which corresponds to a percolation network model with the occupation factor being equal to $p(\mathrm{Ni})$. In the initial step for this simulation, the spatial long-range correlation decay κ is kept zero without easy axis rotation. The simulated distributions of local fields at the muon EPsite using the Monte Carlo method with different site populations $p(\mathrm{Ni})$ are shown in Fig. 8. The average internal field is largely reduced by Ni site dilution, with several discrete peaks of the field strengths, which can be attributed to the occupancies of Ni in the nearest neighbor(NN) sites, next NN sites, etc. The corresponding ZF-μSR time spectra for these percolation field distributions are simulated by a convoluting function $G(t, |B|) = \frac{2}{3}\cos(\gamma_\mu |B| t) + \frac{1}{3}$ with the probability distributions derived from the simulated field distributions. As shown in Fig. 9, the simulated ZF-μSR time spectra evolve from an underdamped to an overdamped case with decreasing $p(\mathrm{Ni})$. For $p(\mathrm{Ni}) = 0.4$ [panel (c)], the
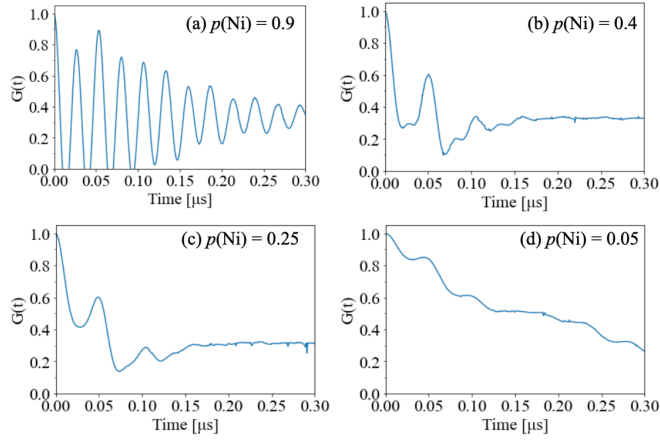
FIG. 9. The simulated ZF-μSR time spectra in the case of Ni site "simple dilution" as in the percolation network with the site population (a) $p(\text{Ni}) = 0.9$, (b) 0.4, (c) 0.25, and (d) 0.05.

spectrum starts to display a Lorentizen-like decay feature, similar to the actual μSR spectrum evolution observed with Se doping as shown in Fig. 2. After involving easy axis randomization, the multipeak field pattern is smeared out and broadened as shown in panel (a) of Fig. 10, and the generated ZF time spectra with $p(\text{Ni}) = 0.4$ [panel (b)] becomes closer to the observed time spectra for $x = 0.5$ and 0.6 samples of NiS$_{2-x}$Se$_x$ system [green and dark blue in Fig. 2(b)]. In addition to the easy axis tilting, a finite inverse correlation length κ would further broaden and smear the field pattern and thus making the resulting μSR spectrum even closer to the observed ones.

Thus an Ni moment dilution factor $p(\text{Ni}) \sim 0.4$ together with the easy axis randomization will broaden the field distribution at the muon EPsite significantly, and also reduce the average field by $\sim 60\%$, making the μSR spectrum close to the observed ones for $x = 0.5$ and 0.6 samples. For the neutron scattering results, under the "simple dilution" model of Ni moments, neutron Bragg intensity will be reduced as $p(\text{Ni})$ decreases, whereas the Bragg peak width will remain unchanged unless the correlation length changes. The easy axis tilting will not change the neutron intensity. Although the simulation result of Ni site dilution qualitatively agrees with the neutron intensity results, we note here that a $p(\text{Ni}) \sim 0.4$ will reduce the average neutron static moment to 0.4 times the value expected for NiS$_2$ with a perfect lattice. This is not in

agreement with the observed neutron results summarized in Fig. 6(a), showing 0.5 $\sim$0.6 moment sizes of the NiS$_2$. This might be due to reasons beyond this Ni dilution model, such as an interplay between the M1 and M2 spin structure in the AFI region. In summary, we have shown that the combination of percolation and easy axis orientation can qualitatively explain the neutron and muon results, resolving the main apparent contradiction between the sharp neutron Bragg peak and a highly random muon local static fields.

V. CHARGE AND SPIN PERCOLATION ANALYSES

A. Motivating results

A possible division of different species of Ni atoms with different moment sizes, depending on the occupation of S or Se surrounding Ni, was discussed in 1976 by Krill *et al.* [25] related to their results on ^{61}Ni Mössbauer effect in Ni(S, Se)$_2$. Although their data was not sufficient for verifying this situation, and the authors did not explicitly discuss in terms of the charge or spin percolation, this paper marks a pioneering conceptual contribution in considering nonuniform Ni moment size in Ni(S, Se)$_2$. The first direct experimental results which hinted at the percolation-like situation for NiS$_{2-x}$Se$_x$ system were obtained by Iwaya *et al.* [28] in 2004, who used STM and reported microscopically inhomogeneous responses of local conductance in $x = 0.5$ specimens in the AFM state close to the MIT boundary. In the previous section, we provided new data and analyses favoring the percolation picture based on the comparison of muon and neutron results. In this section, we propose a charge-spin percolation model for explaining the AFI to AFM to PMM states phase transitions in the NiS$_{2-x}$Se$_x$ system. The basic idea is that the MIT is due to the bond percolation of metallic Ni-Se-Ni (and Ni-Se-Se-Ni) connection, while the magnetic order of the AFM phase is supported by a still surviving network of remaining Ni with localized moments. When this spin percolation network loses connection, the system evolves into the PMM phase.

Regarding the charge percolation, H.J. Noh [29] recently proposed a model considering the metallic connection among NiX$_6$ (X = S or Se) octahedrons via the formation of Se-Se dimers, and estimated the percolation threshold of metallic connection at $x = 0.55$, which is reasonably close to the observed value of $x \sim 0.45$. On the other hand, an elaborate XRD structural study [34] reported that the local distance between Ni and chalcogen atoms changes significantly at the MIT, while no anomaly was detected for the distance between the chalcogen-chalcogen dimer. Therefore, here we develop a model which takes into account the direct connections between nearest Ni atoms through Se.

B. Our model and simulation of charge percolation

Figure 11(a) illustrates the NiS$_{2-x}$Se$_x$ crystal structure. Each Ni is surrounded by six chalcogen atoms. In our model, we assume that S (dark blue atoms) and Se (red atoms) are randomly distributed on the chalcogen sites for a Se concentration x value, with each site having a probability $p(\text{Se}) = \frac{x}{2}$ of being Se, and thus $1 - \frac{x}{2}$ of being S. Each Ni-Se bond is assumed to be conductive with a probability q, while all the other bonds are insulating. In this case, the nearest neighbor
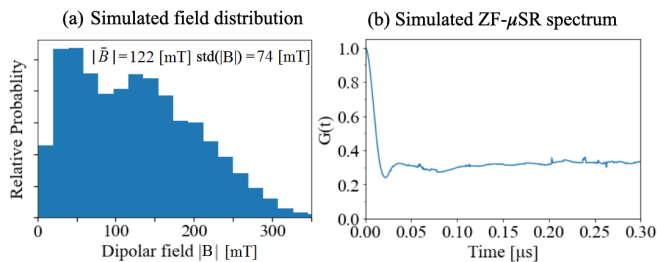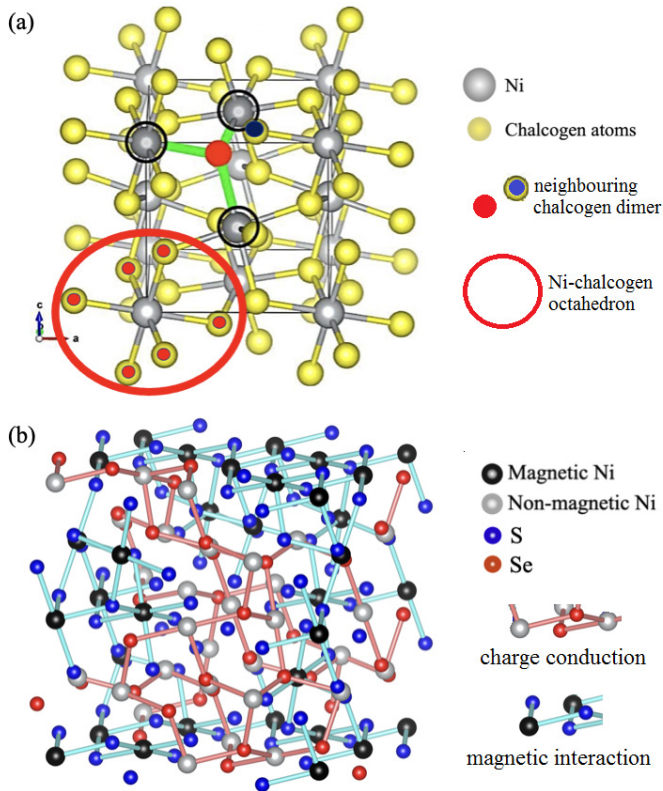

FIG. 10. (a) The simulated field pattern and (b) The simulated time spectrum in the case of $p(\text{Ni}) = 0.4$ and easy axis randomization.

FIG. 11. (a) Pyrite structure of $NiS_{2-x}Se_x$, with each Ni (gray) connected to 6 chalcogen atoms (yellow). The red sphere and green bonds show that one chalcogen atom is connected with three Ni atoms. The structure inside the red circle represents a NiX_6 (X = S or Se) octahedron. (b) Diagram of the proposed charge spin percolation model of $NiS_{2-x}Se_x$ made by VESTA [35] showing a random distributed Se pattern at $p(Se) = 0.3$ ($x = 0.6$). Blue and red atoms represent S and Se, respectively. Black and gray atoms represent magnetic Ni and nonmagnetic Ni, respectively. The red and blue clusters correspond to the Ni-Se (metallic) and Ni-S (magnetic) clusters, respectively. The lattice is in percolating state if a vertically spanned cluster can be found.

Ni atoms can be connected via Ni-Se-Ni paths (red bonds), and a group of Ni atoms connected by Ni-Se-Ni bonds can form an infinite metallic cluster, so the lattice is considered to be in a percolating metallic state. The simulated percolating probability was calculated using the Monte Carlo method by performing $\geqslant 10\,000$ independent trials, where the percolation is achieved if there is a connected path that spans the lattice vertically. The resulting percolating probability versus the Se fraction $p(Se)$ for different three-dimensional $L \times L \times L$ lattice sizes with the Ni-Se bond conduction probability $q = 1$ are shown by the solid lines in Fig. 12(a). As the lattice size increases, the percolation probability curves show a more abrupt change, with the percolating threshold $p_{th}(Se) \sim 0.16$. Furthermore, if Se-Se bonds are also assumed to help metallic conductivity, in which case the nearest neighbor Ni atoms can be connected via both Ni-Se-Ni and Ni-Se-Se-Ni paths, the percolating threshold $p_{th}(Se)$ slightly decreases to ~ 0.15, as shown by the dashed lines in Fig. 12(a).

With the conduction probability of an Ni-Se bond $q < 1$, as shown in Fig. 12(b), if the Se-Se bonds are not connected,

the simulated percolation threshold value $p_{th}(Se)$ for $L = 20$ lattice is found to be in good agreement with the MIT point $x_c \sim 0.45$ [$p_{th}(Se) \sim 0.2$] at $q \sim 0.8$. If Se-Se bonds are connected, as shown in Fig. 12(c), the results also show good agreement with the x_c at $q \sim 0.8$. Thus it is found that whether the Se-Se bond is metallic or not, the conclusion of this charge percolation model is not significantly altered. This feature is consistent with the previous structural study [34] on the bond distance change at the MIT.

C. Spin percolation simulation

For the spin percolation part, magnetic Ni atoms are identified as those surrounded by more than five S atoms in the NiX_6(X = S or Se) octahedron. A Ni surrounded by six S atoms is isolated from the metallic cluster ("isolated Ni") and an Ni surrounded by one Se and five S atoms is connected to the metallic cluster but as a "dangling end" ("dangling Ni"). When those magnetic Ni atoms (black atoms in Fig. 11) form an infinite magnetic cluster via Ni-S-Ni [light blue bonds in Fig. 11(b)], the lattice is considered to be in the magnetically ordered state. A simpler but conceptually similar analysis was described in Ref. [25].

Monte Carlo simulations were performed to predict the magnetic Ni percolation threshold, and the resulting magnetic percolating probability with different Se fraction $p(Se) = x/2$, shown in Fig. 12(d), exhibits a percolation threshold $p_{th}(Se) \sim 0.45$, corresponding to the disappearance of magnetic order at Se content $x \sim 0.9$. This value is close to the actual magnetic transition at $x \sim 1.0$. The calculated population of magnetic Ni in the largest cluster and the total population of magnetic Ni are shown in Fig. 12(e), which are in qualitative agreement with the static internal field observed by μSR for the AFM region as shown in Fig. 6(c). As shown in Fig. 12(f), the proposed percolation model can explain the observed AFI to AFM transition at $x \sim 0.45$ and AFM to PMM transition as $x \sim 1.0$ as the charge and spin connections of the interpenetrating percolating spin and charge networks, illustrated in Fig. 11(b).

D. Comparisons with Hall effect

Furthermore, we estimated the Hall effect for $NiS_{2-x}Se_x$ in our percolation model by making the following assumptions. (1) Each Ni can contribute up to one itinerant charge at most. (2) Magnetic Nis cannot contribute to metallic conduction. (3) Total number of carriers per unit volume can be estimated by the lattice constant of 5.67 Å [24] with four Ni atoms per unit cell in FCC configuration. The carrier density n_c is calculated as $1 - $ (magnetic Ni)/(total Ni) and then compared with the absolute values of the measured Hall coefficients reported in Ref. [20]. As shown in Fig. 13, the simulation and experimental results are in good agreement not only on the curvature but also on the absolute values of the itinerant carrier density.

E. Comparisons with muon and neutron results and Néel temperature

To systematically compare the percolation model and experimental results, Fig. 14 presents the simulation results of
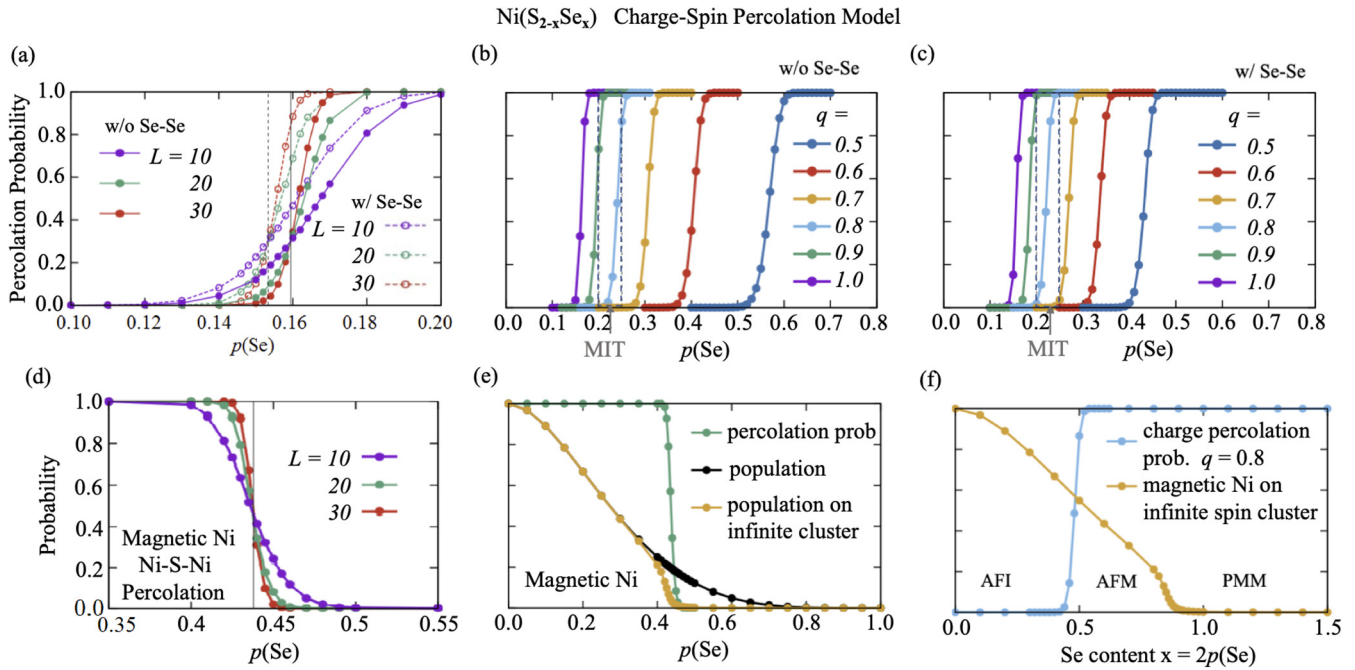
FIG. 12. (a) Monte Carlo simulation checking the charge bond percolation threshold $p_{\rm th}$(Se) for different lattice size $L{\times}L{\times}L$, without Se-Se connection (solid lines) and with Se-Se connection (dashed lines). [(b) and (c)] The charge bond percolation probability curves for different conduction probability q of Ni-Se bond without Se-Se connection (b) and with Se-Se connection (c). (d) Monte Carlo simulation checking the percolation threshold $p_{\rm th}$(Se) of magnetic Ni site percolation for different lattice size L. (e) Magnetic Ni population curve and crossing probability curve of magnetic Ni. (f) Phase diagram based on the percolation model for MIT and magnetic phase transition. The error bars are smaller than the size of the symbols.

the proposed charge-spin percolation model together with experimental results of neutron scattering, μSR, and the magnetic ordering Néel temperature T_N as a function of Se concentration x. The ordered Ni moment size derived from the magnetic Bragg peak intensity of neutron scattering is shown by the red closed symbols, with the Ni moment size for the pure compound NiS₂ being $1.0 \sim 1.2\mu_B$ [22–24] as shown by the red vertical axis. In the region of $x = 0.5$–0.7, a reasonable agreement is found between the percolation model (yellow open triangles) and neutron intensity. For the region with x closer to the disappearance of magnetic order at $x \sim 0.9$, we note that the neutron data exhibits some scattering, and thus further experimental data are required for reliable comparisons.
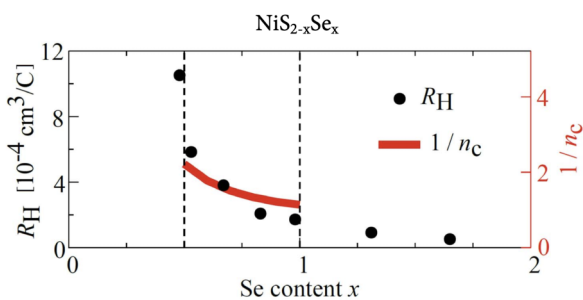
To compare the μSR results with the percolation model, we assumed the magnetic order of the percolating magnetic infinite cluster with the magnetic Ni site population of p(Ni) $= 0.4$ for Se concentration $x = 0.6$, as predicted by the
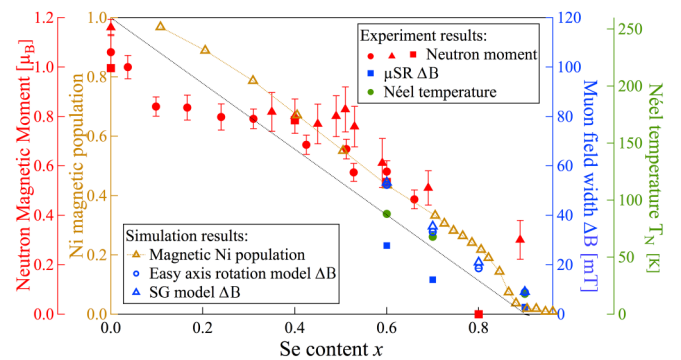

FIG. 13. Hall coefficients adapted from Miyasaka *et al.* (Ref. [20]) compared to the percolation model simulated results (red line).

FIG. 14. Comparison of experimental results (closed symbols) and simulation results (open symbols) of NiS₂₋ₓSeₓ system. Se concentration dependence of Ni magnetic population calculated from the percolation model (yellow open triangles); neutron magnetic moment (red closed symbols) data adapted from Miyadai *et al.* [22] (red closed circles), Matsuura *et al.* [23] (red closed triangles) and Yano *et al.* [24] (red closed squares); observed μSR field width ΔB in the AFM region (blue closed squares); the simulated muon field width ΔB with Ni site percolation (blue open symbols) for the easy axis rotation model (blue open circles) and the spin-glass model (blue open triangles); magnetic ordering temperature T_N in the AFM region (green closed circles).

percolation model (yellow open triangles). Then we calculated the internal field distribution for 90° easy axis randomization. The ΔB of the muon internal field from this simulation was obtained by fitting the simulated μSR time spectra with $G(t) = \frac{1}{3} + \frac{2}{3}(1 - at)e^{-at}$ to get the relaxation rate a, and $\Delta B = a/\gamma_\mu$. The expected μSR field width ΔB for a magnetic Ni moment size of $0.986\mu_B$ on the infinite magnetic cluster is shown by the blue open circle symbol in Fig. 14 at the corresponding magnetic Ni population concentration. Similar calculations were also performed for $p(\text{Ni}) = 0.3, 0.2$, and 0.1, which correspond to Se concentration $x = 0.7, 0.8$, and 0.9 according to the percolation model prediction, and the results are shown by the same blue open circle symbols.

It is also possible to estimate the μSR field width ΔB for the spin-glass (SG) model where completely random spatial spin correlations are assumed among magnetic Ni moments on the infinite cluster. We note here that the spin-glass model does not support any Bragg peak in neutron scattering, but the actual spin structure near the magnetic percolation threshold might become closer to the SG situation. The results for the SG simulation, shown by the open blue triangle symbols in Fig. 14 indicate that the expected μSR widths are very close between the easy-axis randomized AF percolation model and the SG model. The simulated μSR time spectrum and the fitting lines of these two models discussed above can be found in Appendix B. Compared to these predictions, the observed μSR results shown by the blue closed circle symbols in Fig. 14 are significantly lower, but with the concentration dependence qualitatively similar to the simulation, exhibiting disappearance of the width at $x = 1.0$.

The percolation model is also compared with the ordering temperature variation with $x > 0.6$. The pure compound point $x = 0$, $y = 1.0$ and the percolation point $x = 0.9$, $y = 0$ are connected by the black dashed line, and the Néel temperature T_N of $x = 0.6$ sample is plotted as the green closed circle symbol on the line in Fig. 14. Then we plot other points of T_N for $x > 0.6$ of the NiS$_{2-x}$Se$_x$ system. In the region with $x \geqslant 0.7$, the ordering temperature points lie lower than the Ni population yellow line. This is analogous to the case of (Mn, Zn)F$_2$ [36], where T_N shows some reduction from the percolation model population line of the BCC percolating magnet. In the NiS$_{2-x}$Se$_x$ system, the ordering temperature T_N and the muon field width ΔB both exhibit a significant reduction compared to the variation of magnetically connected Ni population. The reduction of T_N can be ascribed to the reduction of the spin-wave stiffness constant, which represents the energy scale of dynamic spin excitations [36].

The reduction of the μSR relaxation rate from the value obtained for the full Ni moment is likely indicating the reduction of the individual ordered Ni moment size. In the case of suppression of magnetic order in low-dimensional and/or frustrated spin systems, both the ordering temperature and the individual ordered moment size exhibit reductions near the disappearance of magnetic order, suggesting that thermal and quantum fluctuations both contribute effectively to the destruction of magnetic order. This feature was shown, for example, by an earlier μSR study on quasi 1D magnets in Kojima *et al.* [37]. Very recently, Chakraborty *et al.* [38] performed a percolation simulation on the site-diluted Hubbard model, and reported a reduction of the individual ordered moment size near the percolation threshold where magnetic order is lost. These examples suggest that, near $x = 0.7 \sim 0.9$ of the NiS$_{2-x}$Se$_x$ system, one may expect a significant reduction of the individual Ni ordered moment size, as well as the gradual destruction of long-range spin correlations on the magnetic Ni infinite cluster.

In summary, the proposed interpenetrating charge and spin percolation model of NiS$_{2-x}$Se$_x$ can successfully explain: (1) the Se concentration $x \sim 0.45$ of MIT as the result of percolation of the charge conduction path through Ni-Se bonds; (2) the Se concentration $x \sim 1.0$ of AFM to PMM variation as the spin percolation with the infinite cluster of isolated and dangling Ni connected by Ni-S-Ni bonds; (3) variation of neutron Bragg peak intensity with $x = 0.4$–0.7; (4) absolute values of the Hall effect with $x = 0.5$–1.0; (5) qualitative variation of the muon spin relaxation rate with $x = 0.6$–0.9; and (6) variation of the ordering temperature T_N with $x = 0.6$–0.9. This model is also consistent with the STM observation of the microscopic variation of the local conductance for $x = 0.5$. Thus we propose the interpenetrating charge spin percolation as a new model to explain the process of AFI to AFM to PMM evolution in the Mott transition of NiS$_{2-x}$Se$_x$ system.

VI. DISCUSSIONS, CONCLUSIONS AND OUTLOOK

In this investigation, the two-step quantum evolution from AFI to AFM to PMM phases of a Mott system NiS$_{2-x}$Se$_x$ was studied by the μSR technique. Previously-unknown features of static magnetism in the AFM state were revealed. The ZF-μSR results in the intermediate AFM region with $0.6 \leqslant x \leqslant 0.9$ show a spin-glass-like time spectra, indicating highly disordered spin correlations. When approaching the PMM state from the AFM side, the static local moment size is reduced with increasing Se doping while the volume fraction remains nearly full until very close to the PMM phase boundary. This suggests the absence of macroscopic antiferromagnetic-paramagnetic phase separation.

The dipolar field scales with $1/r^3$ to the distance r between the source spin and the muon site. For a 1 μ_B static spin, the dipolar field B_{dip} at $r = 1$ Å distance is ~ 1 T: $B_{\text{dip}}(r = 10 \text{ Å}) \sim 1$ mT, and $B_{\text{dip}}(r = 20 \text{ Å}) \sim 0.13$ mT. The random field of ~ 0.1 mT causes a clearly visible relaxation in ZF-μSR time spectra within the time window of $t \sim 10 \mu$s. This implies that a macroscopic phase separation with a domain size larger than about five lattice constants can be distinguished, and such a situation is ruled out in the present study in the AFM region. Thus the magnetic order in Ni(S, Se)$_2$ is destroyed by the reduction of static local ordered moment size without the suppression of antiferromagnetic volume fraction.

This behavior is different from the suppression of the volume fraction previously found in the Mott systems V$_2$O$_3$, RENiO$_3$ [11] and BaCoS$_2$ [13]. In contrast to the strongly first-order feature in V$_2$O$_3$ and RENiO$_3$, potentially related to the simultaneous structural phase transition at MIT, the percolation process in Ni(S, Se)$_2$ may have provided help for the system to avoid such an abrupt change and promoted the AFM region as the compromise between the charge and spin order features of Mott transition. The absence of critical spin dynamics observed in $1/T_1$ suggests a first-order

thermal phase transition in NiS$_{2-x}$Se$_x$. In magnetic percolation models, one would expect a second-order transition for the magnetic order of the infinite cluster. The absence of the sharp critical behavior suggests that the magnetic order in the AFM state of Ni(S, Se)$_2$ may be more complicated with some factors smearing the critical behavior.

We performed dipolar field simulations on NiS$_{2-x}$Se$_x$ to reconcile the seemingly contradicting experimental results of previous neutron scattering and μSR in the AFM region: AF Bragg peaks are persistently observed by neutron scattering, while μSR exhibits spin-glass-like time spectra expected for highly random spin structures. We found that only the combination of Ni magnetic site dilution and easy axis rotation/randomization can lead to the Lorentzian-like field distribution observed by μSR. Both the easy axis rotation and dilution will suppress and broaden the field at the muon site but not affect the neutron Bragg width. These features would help reconcile the seemingly contradicting neutron and muon results. This provides a useful example and a new concept when one compares muon and neutron results in other magnetic materials.

In general, different time windows of neutron and muon measurements could possibly influence the comparison of the estimated moment sizes. Based on the discussion given in Appendix. C, we argue that there is no dependence of the "static" Ni moment values on the time scales of the probes in the present case. We therefore cannot consider that the remaining difference in the static moment size estimated by neutrons and muons, shown in Fig. 14, is caused mainly by the time window effect. Further effort is required to understand the origin of this difference.

In 1976 [25], ^{61}Ni Mössbauer effect results were reported with the suggestion of possible inhomogeneous distribution of Ni moment size in Ni(S, Se)$_2$, while another study of ^{57}Fe Mössbauer effect in 1978 [26] claimed more homogeneous distribution of Ni moment size. In our view, these results are very interesting, but statistical accuracy seems to be insufficient for determining details of the situation. Renewed future efforts on Mössbauer experiments of both ^{61}Ni and ^{57}Fe with significantly improved statistics on high-quality specimens could provide further detailed and direct information on the distribution of Ni moment size in the AFM region of Ni(S, Se)$_2$.

The detailed magnetic order information derived from μSR experimental results and the Ni site dilution simulations further motivated us to propose a model based on interpenetrating charge and spin percolation networks. That model captures the observed results in Se concentrations x for AFI to AFM and AFM to PMM transitions, qualitative features of x-dependence of the muon and neutron results, Hall coefficient, and Néel temperature in the AFM state, and spatial inhomogeneity of the STM results at $x = 0.5$. These represent perhaps one of the most detailed experimental results and model pictures available among systems showing the two-step Mott transitions. We shall remind that a similar two-step transition takes place when hydrostatic pressure is applied to pure NiS$_2$. Although similarities in transport [20] and optical conductivity [27] results have been pointed out between the (S,Se) tuning and pressure tuning, the lack of neutron and muon results in hydrostatic pressure prevents further detailed

comparisons between these two different tunings. Since the Se and S distinction does not exist in the pressure tuning of NiS$_2$, the present percolation model may require a significant modification before being applied to the case of pressure tuning. In this way, the present results do not necessarily represent the situation of two-step Mott transitions in general. We simply provided an account for a particular case of Ni(S, Se)$_2$.

One possible direction to extend the percolation model is to see its applicability to the AFI region. In this region, the geometrical frustration of FCC antiferromagnet leads to the energetic degeneracy of the M1 and M2 spin configurations. The (S,Se) substitutions may lift this degeneracy, which could result in an increase of the ordering temperature with increasing Se concentration x in the AFI region. The present model of charge and spin percolation is a simple classical model. More microscopic theoretical accounts on the metallicity of Ni-Se-Ni and magnetic exchange interaction of Ni-S-Ni connections, using DMFT or other advanced methods, would provide a further basis for the present proposal.

APPENDIX A: COMPARISONS BETWEEN THE ZF-μSR TIME SPECTRA FROM NiS$_{2-x}$Se$_x$ WITH $x = 0.5$ AND 0.6

Figure 15 compares the ZF-μSR time spectra from NiS$_{2-x}$Se$_x$ with $x = 0.5$ and 0.6 at $T \sim 2$ K. The spectrum
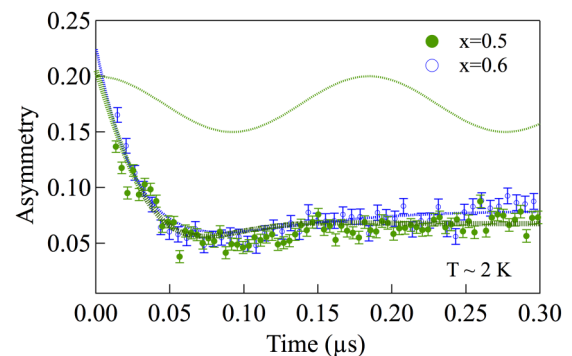

FIG. 15. The ZF-μSR time spectra from NiS$_{2-x}$Se$_x$ with $x = 0.5$ and 0.6 at $T \sim 2$ K.
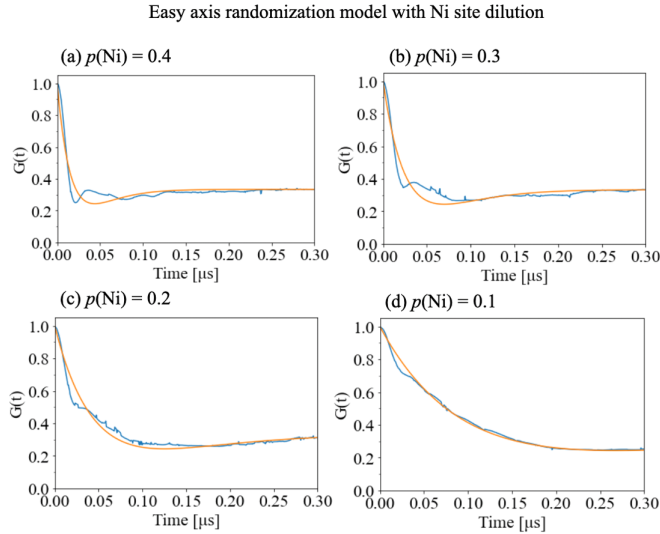
Easy axis randomization model with Ni site dilution

FIG. 16. The easy-axis randomization model with Ni site dilution. Blue lines show the simulated μSR time spectrum in the case of Ni site dilution and $90°$ easy-axis randomization. The spectrum are fitted by Eq. (B3), shown by the yellow lines in each graph, for different magnetic Ni population with (a) $p(\mathrm{Ni}) = 0.4$, (b) 0.3, (c) 0.2, and (d) 0.1, which correspond to Se content $x \approx 0.6, 0.7, 0.8$, and 0.9, respectively, according to the prediction of our percolation model shown in yellow in Fig. 12(e).

for the $x = 0.5$ compound, shown by the green color, exhibits a small oscillatory component superimposed on the simple decay line shape of the spectrum for the $x = 0.6$ compound shown by the blue open symbols. The frequency of this oscillatory component is illustrated by the solid line in the upper part of the figure.

APPENDIX B: SIMULATED μSR SPECTRA

From the field distribution histogram calculated by the Monte Carlo method, the field distribution function $P(|B|)$ can be derived. Thus the ZF-μSR time spectra for this percolation field distribution can be simulated by convolute function $G(t, |B|)$ with the probability distribution

$$G(t) = \int_0^{|B|_{\max}} G(t, |B|)P(|B|) \, d|B|, \quad \text{(B1)}$$

where

$$G(t, |B|) = \frac{2}{3} \cos{(\gamma_\mu |B| t)} + \frac{1}{3}. \quad \text{(B2)}$$

Then the simulated ZF-μSR time spectra is fitted by the "spin-glass" function

$$G(t) = \frac{1}{3} + \frac{2}{3}(1 - at)e^{-at}, \quad \text{(B3)}$$

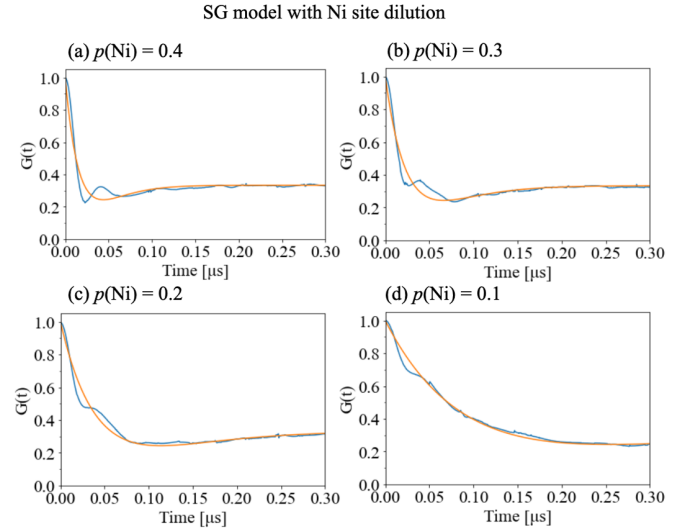as shown by the yellow lines in Figs. 16 and 17.

SG model with Ni site dilution

FIG. 17. The spin-glass model with Ni site dilution. Corresponding μSR spectrum and fitting lines as shown in Fig. 16, but under the spin-glass model with Ni Site dilution.

APPENDIX C: EFFECT OF DIFFERENT TIME WINDOWS OF MUON AND NEUTRON MEASUREMENTS ON THE ESTIMATE OF THE STATIC NI MOMENT SIZE

Typically, when short- range and slow spin fluctuations exist, neutron intensity integrates over a wider energy region as compared to muon static field which is defined by the time scale of 10 to 1000 ns. In the present case, however, both the neutron Bragg peak intensity and μSR local field can be regarded as representing the same genuine "static" order due to the following three reasons. (1) The Bragg peak is very sharp in momentum space, with the spin correlation length exceeding 50 Å$\sim$10 lattice constants. The correlated region then includes more than 1000 ordered Ni spins, which guarantees the fluctuation time scales to give the energy width smaller than $\sim J/1000 \sim 1.5 \times 10^{-2}$ meV, where J is the AF exchange interaction between Ni moments [30]. Hence the Bragg peak is very sharp not only in momentum space but also in energy space. (2) From the μSR $1/T_1$ measurements shown in Fig. 5, one can crudely estimate the lower limit of the quasi-elastic spin fluctuation rate ν by using the well-known relationship for the narrowing limit $1/T_1 \sim \omega^2/\nu$, where $\omega \sim 230 \, \mu s^{-1}$ is the instantaneous magnitude of the fluctuating local field at the muon site inferred from the static local field of pure NiS_2 at $T \to 0$. Typical values of $1/T_1 < 0.01 \, \mu s^{-1}$ in the $Ni(S, Se)_2$ samples in the AFM region then correspond to $\nu > 5.3 \times 10^6$ μs^{-1}, which would give the energy width in neutron scattering exceeding 3.1 meV. The energy resolutions used in the neutron scattering studies on $Ni(S, Se)_2$ [22–24] are much smaller than this value. In this situation, any possible quasi-elastic spin fluctuations can be distinguished from the elastic Bragg peak. (3) The ^{61}Ni Mössbauer effect study [25] reported the averaged static Ni moment size consistent with the values reported by neutrons shown in Fig. 6(a). This further indicates that there is no dependence of the "static" Ni moment values on the time scales of the probes in the present case.

[1] N. F. Mott, *Metal-Insulator Transitions* (Taylor & Francis, 1990).

[2] M. Imada, A. Fujimori, and Y. Tokura, Metal-insulator transitions, Rev. Mod. Phys. **70**, 1039 (1998).

[3] Y. Cao, V. Fatemi, S. Fang, K. Watanabe, T. Taniguchi, E. Kaxiras, and P. Jarillo-Herrer, Unconventional superconductivity in magic-angle graphene superlattices, Science **556**, 43 (2018).

[4] J. A. Alonso, J. L. García-Muñoz, M. T. Fernández-Díaz, M. A. G. Aranda, M. J. Martínez-Lope, and M. T. Casais, Charge Disproportionation in RNiO$_3$ Perovskites: Simultaneous Metal-Insulator and Structural Transition in YNiO$_3$, Phys. Rev. Lett. **82**, 3871 (1999).

[5] S. A. Carter, T. F. Rosenbaum, M. Lu, H. M. Jaeger, P. Metcalf, J. M. Honig, and J. Spalek, Magnetic and transport studies of pure V$_2$O$_3$ under pressure, Phys. Rev. B **49**, 7898 (1994).

[6] M. M. Qazilbash, M. Brehm, B.-G. Chae, P.-C. Ho, G. O. Andreev, B.-J. Kim, S. J. Yun, A. Balatsky, M. Maple, F. Keilmann *et al.*, Mott transition in VO$_2$ revealed by infrared spectroscopy and nano-imaging, Science **318**, 1750 (2007).

[7] A. McLeod, E. Van Heumen, J. Ramirez, S. Wang, T. Saerbeck, S. Guenon, M. Goldflam, L. Anderegg, P. Kelly, A. Mueller *et al.*, Nanotextured phase coexistence in the correlated insulator V$_2$O$_3$, Nat. Phys. **13**, 80 (2017).

[8] S. J. Blundell, R. De Renzi, T. Lancaster, and F. L. Pratt, *Muon Spectroscopy: An Introduction* (Oxford University Press, 2022).

[9] Y. J. Uemura, μSR relaxation functions in magnetic materials, in *Muon Science*, edited by S. L. Lee, S. H. Kilcoyne, and R. Cywinski (Institute of Physics Publishing, London, 1999), Chap. 4, pp. 85–114.

[10] J. B. Torrance, P. Lacorre, A. I. Nazzal, E. J. Ansaldo, and C. Niedermayer, Systematic study of insulator-metal transitions in perovskites RNiO$_3$ (R = Pr,Nd,Sm,Eu) due to closing of charge-transfer gap, Phys. Rev. B **45**, 8209 (1992).

[11] B. A. Frandsen, L. Liu, S. C. Cheung, Z. Guguchia, R. Khasanov, E. Morenzoni, T. J. S. Munsie, A. M. Hallas, M. N. Wilson, Y. Cai, G. M. Luke, B. Chen, W. Li, C. Jin, C. Ding, S. Guo, F. Ning, T. U. Ito, W. Higemoto, S. J. L. Billinge *et al.*, Volume-wise destruction of the antiferromagnetic mott insulating state through quantum tuning, Nat. Commun. **7**, 12519 (2016).

[12] Y. J. Uemura, T. Yamazaki, Y. Kitaoka, M. Takigawa, and H. Yasuoka, Positive muon spin precession in magnetic oxides MnO and V$_2$O$_3$; local fields and phase transition, Hyperfine Interact. **17**, 339 (1984).

[13] Z. Guguchia, B. A. Frandsen, D. Santos-Cottin, S. C. Cheung, Z. Gong, Q. Sheng, K. Yamakawa, A. M. Hallas, M. N. Wilson, Y. Cai, J. Beare, R. Khasanov, R. De Renzi, G. M. Luke, S. Shamoto, A. Gauzzi, Y. Klein, and Y. J. Uemura, Probing the quantum phase transition in mott insulator BaCoS$_2$ tuned by pressure and ni substitution, Phys. Rev. Mater. **3**, 045001 (2019).

[14] G. Krill, M. F. Lapierre, C. Robert, F. Gautier, G. Czjzek, J. Fink, and H. Schmidt, Electronic and magnetic properties of the pyrite-structure compound NiS$_2$: influence of vacancies and copper impurities, J. Phys. C **9**, 761 (1976).

[15] H. Jarrett, R. Bouchard, J. Gillson, G. J. S. Marcus, and J. Weiher, The metal-semiconductor phase diagram for NiS$_{2-x}$Se$_x$, Mater. Res. Bull. **8**, 877 (1973).

[16] S. Friedemann, H. Chang, M. B. Gamża, P. Reiss, X. Chen, P. Alireza, W. A. Coniglio, D. Graf, S. Tozer, and F. M. Grosche, Large fermi surface of heavy electrons at the border of mott insulating state in NiS$_2$, Sci. Rep. **6**, 25335 (2016).

[17] Y. Sekine, H. Takahashi, N. Môri, T. Matsumoto, and T. Kosaka, Effect of pressure on transport properties of Ni(S$_{1-x}$Se$_x$)$_2$, Phys. B: Condens. Matter **237–238**, 148 (1997).

[18] C.-Y. Moon, H. Kang, B. G. Jang, and J. H. Shim, Composition and temperature dependent electronic structures of NiS$_{2-x}$Se$_x$ alloys: First-principles dynamical mean-field theory approach, Phys. Rev. B **92**, 235130 (2015).

[19] C. Schuster, M. Gatti, and A. Rubio, Electronic and magnetic properties of NiS$_2$, NiSSe and NiSe$_2$ by a combination of theoretical methods, Eur. Phys. J. B **85**, 325 (2012).

[20] S. Miyasaka, H. Takagi, Y. Sekine, H. Takahashi, N. Môri, and R. J. Cava, Metal-insulator transition and itinerant antiferromagnetism in NiS$_{2-x}$Se$_x$ pyrite, J. Phys. Soc. Jpn. **69**, 3166 (2000).

[21] Y. Feng, R. Jaramillo, A. Banerjee, J. M. Honig, and T. F. Rosenbaum, Magnetism, structure, and charge correlation at a pressure-induced Mott-Hubbard insulator-metal transition, Phys. Rev. B **83**, 035106 (2011).

[22] T. Miyadai, S. Sudo, Y. Tazuke, N. Môri, and Y. Miyako, Magnetic properties of pyrite type NiS$_{2-x}$Se$_x$, J. Magn. Magn. Mater. **31–34**, 337 (1983).

[23] M. Matsuura, H. Hiraka, K. Yamada, and Y. Endoh, Magnetic phase diagram and metal-insulator transition of NiS$_{2-x}$Se$_x$, J. Phys. Soc. Jpn. **69**, 1503 (2000).

[24] S. Yano, D. Louca, J. Yang, U. Chatterjee, D. E. Bugaris, D. Y. Chung, L. Peng, M. Grayson, and M. G. Kanatzidis, Magnetic structure of NiS$_{2-x}$Se$_x$, Phys. Rev. B **93**, 024409 (2016).

[25] G. Krill, P. Panissod, M. F. Lapierre, F. Gautier, C. Robert, G. Czjzek, J. Fink, H. Schmidt, and R. Kuentzler, Physical properties of compounds NiS$_{2-x}$Se$_x$ with pyrite structure: Metal-non metal transition, evidence for the existence of an antiferromagnetic metallic phase, J. Phys. Colloq. **37**, C4-23 (1976).

[26] Y. Nishihara, S. Ogawa, and S. Waki, Mössbauer study of ^{57}Fe doped in NiS$_{2-x}$Se$_x$-magnetic structure of NiS$_{2-x}$Se$_x$, J. Phys. C **11**, 1935 (1978).

[27] A. Perucchi, C. Marini, M. Valentini, P. Postorino, R. Sopracase, P. Dore, P. Hansmann, O. Jepsen, G. Sangiovanni, A. Toschi, K. Held, D. Topwal, D. D. Sarma, and S. Lupi, Pressure and alloying effects on the metal to insulator transition in NiS$_{2-x}$Se$_x$ studied by infrared spectroscopy, Phys. Rev. B **80**, 073101 (2009).

[28] K. Iwaya, Y. Kohsaka, S. Satow, T. Hanaguri, S. Miyasaka, and H. Takagi, Evolution of local electronic states from a metal to a correlated insulator in a NiS$_{2-x}$Se$_x$ solid solution, Phys. Rev. B **70**, 161103 (2004).

[29] H.-J. Noh, A percolation model for the metal-insulator transition in pyrite Ni(S,Se)$_2$, J. Korean Phys. Soc. **78**, 1191 (2021). For making an agreement with the experiments, this reference introduces the conducting probability on the Ni-Se-S-Ni path in the effective FCC model. This reference shows that if only the Ni-Se-Se-Ni path is assumed without the Ni-Se-S-Ni path, the calculated percolation threshold ($x \sim 0.9$) is much larger than the experimental value ($x \sim 0.45$). The conducting probability of the Se-S bond introduced in this model suppresses the percolation threshold and gives an agreement with the experimental

value. Effectively, the assumption of conductivity of the Ni-Se-S-Ni path in this reference may correspond to making a metallic path via the Ni-Se-Ni in our model proposed in the present paper. These results imply that the Ni-Se-Ni path is important in the charge percolation process.

[30] M. Matsuura, Y. Endoh, H. Hiraka, K. Yamada, A. S. Mishchenko, N. Nagaosa, and I. V. Solovyev, Classical and quantum spin dynamics in the fcc antiferromagnet NiS_2 with frustration, Phys. Rev. B **68**, 094409 (2003).

[31] P. W. Anderson, Generalizations of the weiss molecular field theory of antiferromagnetism, Phys. Rev. **79**, 705 (1950).

[32] A. Suter and B. Wojek, Musrfit: A free platform-independent framework for μ SR data analysis, Phys. Proc. **30**, 69 (2012).

[33] Y. J. Uemura, T. Yamazaki, D. R. Harshman, M. Senba, and E. J. Ansaldo, Muon-spin relaxation in AuFe and CuMn spin glasses, Phys. Rev. B **31**, 546 (1985).

[34] G. Han, S. Choi, H. Cho, B. Sohn, J.-G. Park, and C. Kim, Structural investigation of the insulator-metal transition in $NiS_{2-x}Se_x$ compounds, Phys. Rev. B **98**, 125114 (2018).

[35] K. Momma and F. Izumi, *VESTA3* for three-dimensional visualization of crystal, volumetric and morphology data, J. Appl. Cryst. **44**, 1272 (2011).

[36] Y. J. Uemura and R. J. Birgeneau, Magnons and fractons in the diluted antiferromagnet $Mn_xZn_{1-x}F_2$, Phys. Rev. B **36**, 7024 (1987).

[37] K. M. Kojima, Y. Fudamoto, M. Larkin, G. M. Luke, J. Merrin, B. Nachumi, Y. J. Uemura, N. Motoyama, H. Eisaki, S. Uchida, K. Yamada, Y. Endoh, S. Hosoya, B. J. Sternlieb, and G. Shirane, Reduction of Ordered Moment and Néel Temperature of Quasi-One-Dimensional Antiferromagnets Sr_2CuO_3 and Ca_2CuO_3, Phys. Rev. Lett. **78**, 1787 (1997).

[38] S. Chakraborty, A. Mukherjee, and K. Pradhan, Antiferromagnetism beyond the classical percolation threshold in the diluted half-filled one-band Hubbard model in three dimensions, Phys. Rev. B **106**, 075146 (2022).